

Extreme outflow of Enormous Ly α Nebula in MAMMOTH-1

Shiwu Zhang¹ and Zheng Cai¹

¹*Department of Astronomy, Tsinghua University, Shuangqing Road No.30, Haidian Beijing China*

Abstract

KCWI has a high throughput from 3800 – 4500, optimal for probing Ly α CIV and HeII lines at $z \approx 2$. (2) KCWI has a high spectral-resolution modes ($R > 4000$) which can resolve the gas kinematics and (3) KCWI has a relatively large field-of-view (FoV) to cover extended Ly α nebulae. Furthermore, KCWI nicely complements the characteristics of MUSE which thrives at $\lambda > 5000$. Data was taken with the Keck/KCWI instrument in November 2017. The seeing varied in the range of 0.7-1.1 arcsec.

1. Introduction

It has been realized over the past decade that the black hole at the centre of a galaxy bulge is no mere ornament but may play a major role in galaxy evolution. The process by which this occurs is known as AGN (Active Galactic Nucleus) feedback and it takes place through an interaction between the energy and radiation generated by accretion onto the massive black hole and the gas in the host galaxy. The possibility arises where the intense flux of photons and particles produced by the AGN sweeps the galaxy bulge clean of interstellar gas, terminates star formation, and through lack of fuel for accretion, terminates the AGN. However, the ratio of the size of the black hole to host galaxy is tiny and similar to coin in comparison to the Earth. How can the black hole influence the its host galaxy? The details are still not fully understood and observational evidence is not complement.

Theoretical models of galaxy formation have found it necessary to implement AGN ‘feedback’ processes, during which AGN activity injects energy into the gas in the larger scale environment, in order to reproduce the properties of local massive galaxies, intracluster gas and the intergalactic medium (e.g. BH mass–spheroid mass relationship; the sharp cut-off in the galaxy luminosity function; colour bimodality; metal enrichment; X-ray temperature–luminosity relationship). Placing observational constraints on how AGN activity couples to the gas in galaxies and haloes, and where these processes are most prevalent, is an important area of ongoing research.

2. Observations

In this section, we provide details on the KCWI instrument configurations, observations, data reduction pipeline, and post-processing after standard reduction pipeline

2.1. KCWI Instrument Configuration

Keck Cosmic Web Imager (KCWI) is a general purpose, optical IFS that has been installed on the 10m Keck II telescope. KCWI provides seeing-limited imaging from the wavelength of 3500 – 5700, and the spectral resolution can be configured from $R=1000$ to $R=20000$. The field of view is $20'' \times 33''$ for large slicer, $16'' \times 20''$ for medium slicer and $8'' \times 20''$ for the small slicer. KCWI is optimal for a survey of gaseous nebulae at $z \approx 2$ because: (1)

3. Results

3.1. Radio Emission

Deep VLA observation on MAMMOTH-1 with 2.3" resolution (see in Emonts et al. (2019)) shows radio CO(1-0) emission which trace the cold molecular gas ($T \approx 10$ -100 K) on the central source of MAMMOTH-1 (we use the terminology in Cai et al. (2017) and call it source-B in following sections) and its companions. He used D-configuration of VLA and centered on the frequency of 34.808 GHz ($\nu_{rest}=115.27$ GHz). After 14 hrs exposure, the results shows extended peak radio flux which has 5 kpc offset from the stellar body of source-B (30 kpc beyond 3σ). Besides, he also detected 3 faint radio sources in the same region. With CO(1-0) emission he calculated the total mass of molecular gas $M_{H_2} = 1.4 (\alpha_{CO}/3, 6) \times 10^{11} M_{\odot}$, furthermore, he found an unusually narrow velocity dispersion (FWHM 85 km/s), follows diffuse light seen in HST imaging, he interprets that this molecular CGM in the core likely originated from gas cooling in an enriched multi-phase medium.

From the results of Emonts et al. (2019), we doesn't get any confident detection of continuum radio source at the position of Source-B. However, we give an upper limit on its submillimeter emission, $f_{\nu} < 0.01 mJy$ at $\lambda_{obs} = 8500 \mu m$. But from the results of Arrigoni Battaia et al. (2018) (Fig. 11), this upper limit still cannot rule out the the radio-loud case. But neither the VLA nor ALMA observations detected two distinct radio sources around Source-B, we conclude that Source-B is most likely radio-quiet source.

3.2. Morphology and Emission

Fig. ?? shows the HST image of MAMMOTH-1 with WFC F160W filter and contours for Ly α HeII and CIV emission. All sources marked here are at $z=2.3$ (confirmed by CO(1-0) emission from Emonts et al. (2019) and Qiong (in prep)). It shows Ly α emission extended $> 20''$ which corre-

sponds to $\approx 170\text{kpc}$, this is the typical size of halo at this redshift. It covers all 8 sources here, this indicates that all of these sources could have contribution to illuminate this nebulae. We don't see this nebulae all because FoV of KCWI is $20'' \times 16.8''$ and not that sensitive at the edges. Besides $\text{Ly}\alpha$. Also we see HeII and CIV emission, contour shows signal beyond 3σ and 4σ for these two lines respectively. These two emissions are also extent because their size is larger than seeing and velocity gradient weighted from these 2 lines is significant (we would not see it if they are not resolved). The contour shows these two emission extended $> 6''$ which corresponds to physical projected scale of 50kpc . Besides, We don't find any significant HeII or CIV emission around other sources.

Fig. ?? shows spectra extract in 1 arcsec^2 aperture centering on the flux peaks. We fit the three emission lines with single component gaussian function and also use the central wavelength fitted to calculate their redshifts, moreover we calculate their luminosity beyond 3σ . We show these results and the fitting parameters in Tab. 1.

	$\lambda_c(\text{\AA})$	$\sigma_\lambda(\text{\AA})$	$L(\text{erg/s})$	redshift
$\text{Ly}\alpha$	4024	7	2.68×10^{44}	2.310
HeII	5438	8	1.97×10^{43}	2.316
CIV	5143	13	2.29×10^{43}	2.320

Table 1:

3.3. Kinematics

In this section we present the maps for the flux-weighted velocity centroid and the flux-weighted velocity dispersion of all of the extended emission line to get an indication of the centroid velocity and width of the emission line for each spatial location. Different emission line traces different gas component. We use $\text{Ly}\alpha$ to trace cool gas (10^4K) and use $\text{CIV}(\lambda 1549), \text{HeII}(\lambda 1640)$ emission to trace warm gas (10^5K). These resolved kinematic maps give us the opportunity to detect kinematic patterns, e.g. evidence for rotation, inflows or outflows and help us to have a deep insight look to the physics of this nebula. We filter the spectra with lowpass filter to reduce the noise, this procedure can help us to construct a more clear velocity and velocity dispersion map, we show the results in Fig. ??

Fig. ?? shows the results. Left panel is the continuum-subtracted, pseudo-narrowband image, contour represents the SNR levels. Middle panel shows velocity maps and right panel is velocity dispersion map. $\text{Ly}\alpha$ shows 2 peaks, one is around source-B the other is around G-5, moreover we also see significant velocity gradient close to these 2 peaks in $\text{Ly}\alpha$ velocity map. Besides, dispersion map also reveals relatively large σ_v around these 2 sources. The 2 clues indicate source-B and G-5 both have outflows. To have a deep insight, we bin the data cube with interval length of 200km/s and show the results in Fig. ?. It shows significant separate

red and blue component on either side of source-B. As for G-5, the red component is significant but the blue component is relatively weak.

To further explore the physical mechanism here, we extract spectra from different regions of $\text{Ly}\alpha$ nebula and construct a "spectral map", Fig. ?? shows the result. We construct aperture with radius of 1 arcsec^2 and extract spectra from different part of $\text{Ly}\alpha$ nebulae. We also fit lines with one-component gaussian function and show the fitting parameter in Tab. ?. We clearly see in some regions close to source-B the dispersion is really large even $> 600\text{km/s}$ which corresponds to $\text{FWHM} > 1400\text{km/s}$. It's hard to imagine anything other than an outflow could cause such a large dispersion.

3.4. Model of the outflow

The mass rate, energy rate and momentum rate being carried by outflow are important to help us understand the physical mechanisms to drive it. Although outflow are likely to be entraining gas in multiphases, the cool and warm gas observed here could represent a large fraction of the overall mass and energy of the total outflows. Because of the complication of modeling outflows, here we adopt simple outflow models to provide first order constraints. We calculate the upper and lower limit of the outflow energy rate with 2 different ways and the fiducial value we use is their mean in log space (follow the method given by Harrison et al. (2014)) The upper limit is given by Rodriguez Zaurin et al. (2013), we use eq. 7 in his paper to calculate the mass outflow rate:

$$\dot{M} = \frac{3Lm_p v_{out}}{\alpha_{Ly\alpha}^{eff} h\nu_{Ly\alpha} n_e r} \quad (1)$$

where L is the luminosity of $\text{Lyman}\alpha$ emission, m_p is the proton mass, v_{out} is outflow velocity, $\alpha_{Ly\alpha}^{eff}$ is recombination coefficients, we get this value from Storey & Hummer (1995), $h\nu_{Ly\alpha}$ is the energy of $\text{Lyman}\alpha$ photons, n_e is electron density, r is the distance we see the outflow from the central AGN, in our case we adopt 30kpc . In addition, the kinetic power of the outflow (\dot{E}) is related to the velocity dispersion, mass outflow rate and outflow velocity by:

$$\dot{E} = \frac{\dot{M}}{2} (V_{out}^2 + 3\sigma^2) \quad (2)$$

the main uncertainty in calculating the mass outflow rates is electron density, this value is often measured from the emission-line ratio $\text{SII } \lambda 6716/\lambda 6731$, this doublet is not covered by our IFU observations, hence, we adopt the value in Cai et al. (2017) $n_e = 1.25 \text{ cm}^{-3}$. With this approach, we obtain $\dot{M}_{out,low} \approx 500 M_\odot \text{ yr}^{-1}$. Moreover with the velocity dispersion we estimated, the energy outflow rate is $\dot{E}_{out,low} \approx 10^{44} \text{ erg/s}$.

We also consider the mass energy injection rates assuming an energy conserving bubble in a uniform medium Heckman et al. (1990) which gives the relation:

$$\dot{E}_{out,up} \approx 1.5 \times 10^{46} r_{10}^2 v_{1000}^3 n_{0.5} \text{ erg/s} \quad (3)$$

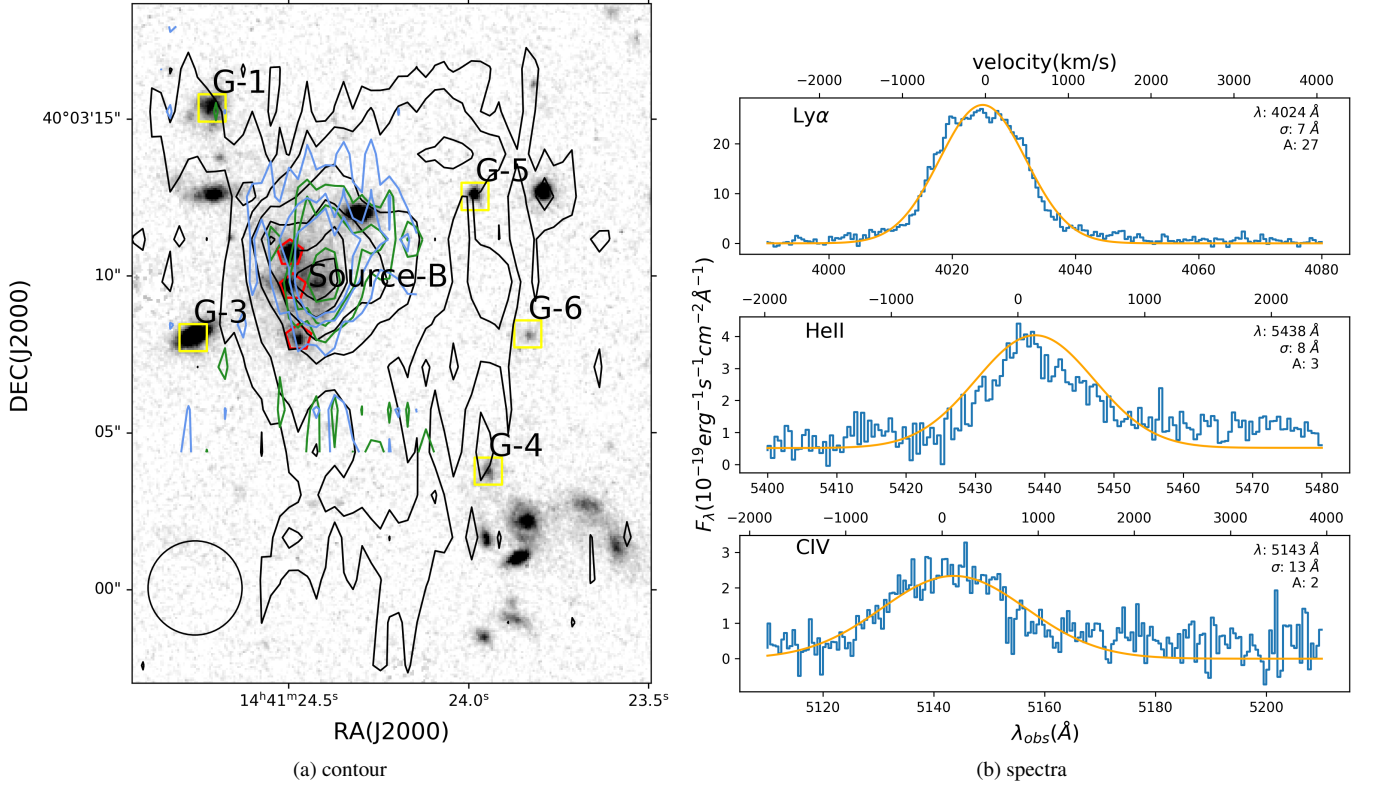


Figure 1: Left: HST image of MAMMOTH-1 from circle 24,25, PI: Cai. We overlay on it $\text{Ly}\alpha$, HeII and CIV pseudo narrow band images. Black contour is $\text{Ly}\alpha$, blue contour is HeII, green contour is CIV. We also mark source-B with red mark and sources at the same redshift with yellow mark. We also plot circle with radius of 1 arcsec^2 . Right: spectra of the 3 emission lines extracted from aperture center on source-B with radius 1 arcsec^2 , we fit them with one-component gaussian function.

Number	1	4	5	7	8	9	10	11	12	13	14	15	16	17	18	19	20	24	25
Velocity(km/s)	-416	-785	-649	-419	-515	-453	208	-157	-257	-424	-211	9	-75	-300	49	236	-267	182	-208
Dispersion(km/s)	618	342	392	626	319	474	450	174	219	444	269	415	799	242	668	481	358	660	472
f_{norm}	0.69	0.63	0.73	0.70	0.79	0.83	0.71	0.84	0.95	0.85	0.91	0.83	0.41	0.86	0.66	0.93	0.81	0.66	0.77

where r_{10} is the radius in unit of 10kpc, v_{1000} in unit of 1000km/s and $n_{0.5}$ is in unit of 0.5 cm^{-3} . Using this method we obtain values of $E_{\text{out,up}} \approx 9 \times 10^{46} \text{ erg/s}$. The mass outflow rates are then given by $\dot{M}_{\text{out,up}} = 2\dot{E}_{\text{out,up}}/c^2$ where c is the speed of light, this gives $\dot{M}_{\text{out,up}} \approx 8.7 \times 10^5 M_{\odot}/\text{yr}$. So the fiducial value we use is $\dot{E}_{\text{out,mean}} = 3 \times 10^{45} \text{ erg/s}$.

Finally, in preparation for the follow discussion, we estimate outflow momentum rate by taking the mass outflow rate calculated above and assuming $\dot{P}_{\text{out}} = \dot{M}_{\text{out}} v_{\text{out}}$

4. Discussion

4.1. What drives the outflow?

In this section we will investigate which of these processes could responsible for driving the extreme outflows observed. The dominant processes that drive such large scale outflow in protocluster and the efficiency to which they are able to couple the gas are currently sources of uncertainty in galaxy formation models. Several possible mechanisms have been suggested to drive galaxy-wide outflows, for example: the stellar

wind and supernovae; radiation pressure from the extremely luminous AGN or star formation; the interaction of radio jets with a clumpy and multiphase interstellar medium; AGN wind initially launched from the accretion disc. Following Harrison et al. (2014), we calculate the coupling efficiency which is a popular method to investigate the likely drivers of large-scale outflow. We compare the ratio of our outflow kinetic energy rate (E_{out}) with (1) the FIR AGN luminosity; (2) the FIR star formation luminosity (these two power are given by Arrigoni Battaia et al. (2018)). We also calculate the momentum-loading factor for both star-forming-driven case and AGN-driven case. Using these results we now explore the possible driving mechanisms to power this outflow.

Fig.?? shows coupling efficiency for both star-forming-driven case and AGN-driven case. We compare our result with results in Harrison et al. (2014). One way for star formation to drive large-scale outflow is by stellar winds or supernovae. An estimation of the coupling efficiency for this case is carried by Kennicutt Jr (1998), he found that the maximum

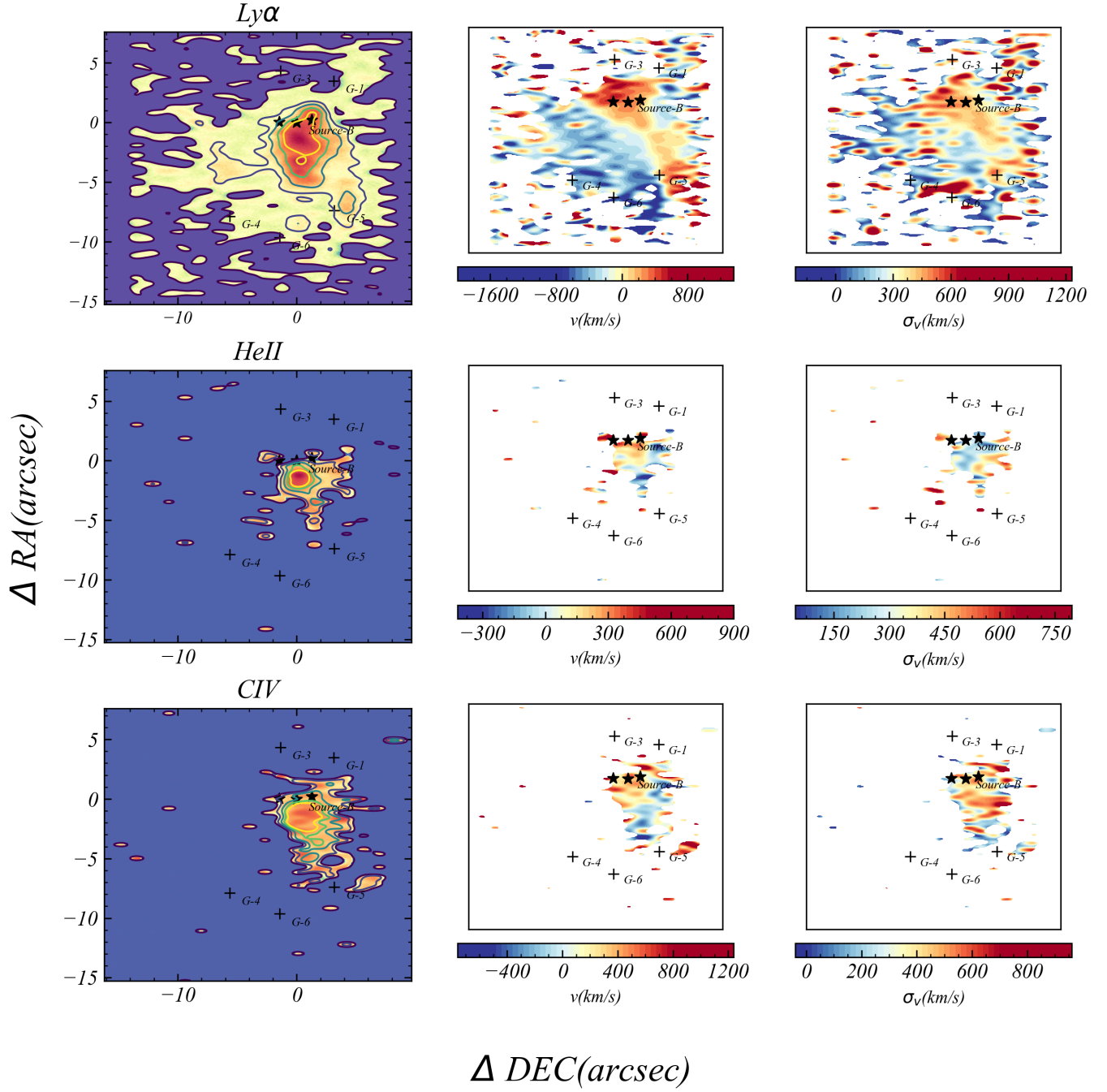


Figure 2: Left: continuum-subtracted pseudo-narrow band images for the 3 emissions. We select regions $> 1.5\sigma$ in each slice and stack these slices together. The contour represent signal-to-noise ratio(SNR), for $Ly\alpha$ is (5 σ , 9 σ , 18 σ , 30 σ , 42 σ , 51 σ), for $HeII$ is (3 σ , 5 σ , 9 σ) and for CIV is (4 σ , 7 σ , 9 σ). Middle: flux-weighted velocity map with respect to the systemic redshift of MAMMOTH-1. Right: flux-weighted velocity dispersion also with respect to systemic redshift of MAMMOTH-1. We also mark sources in the field with cross.

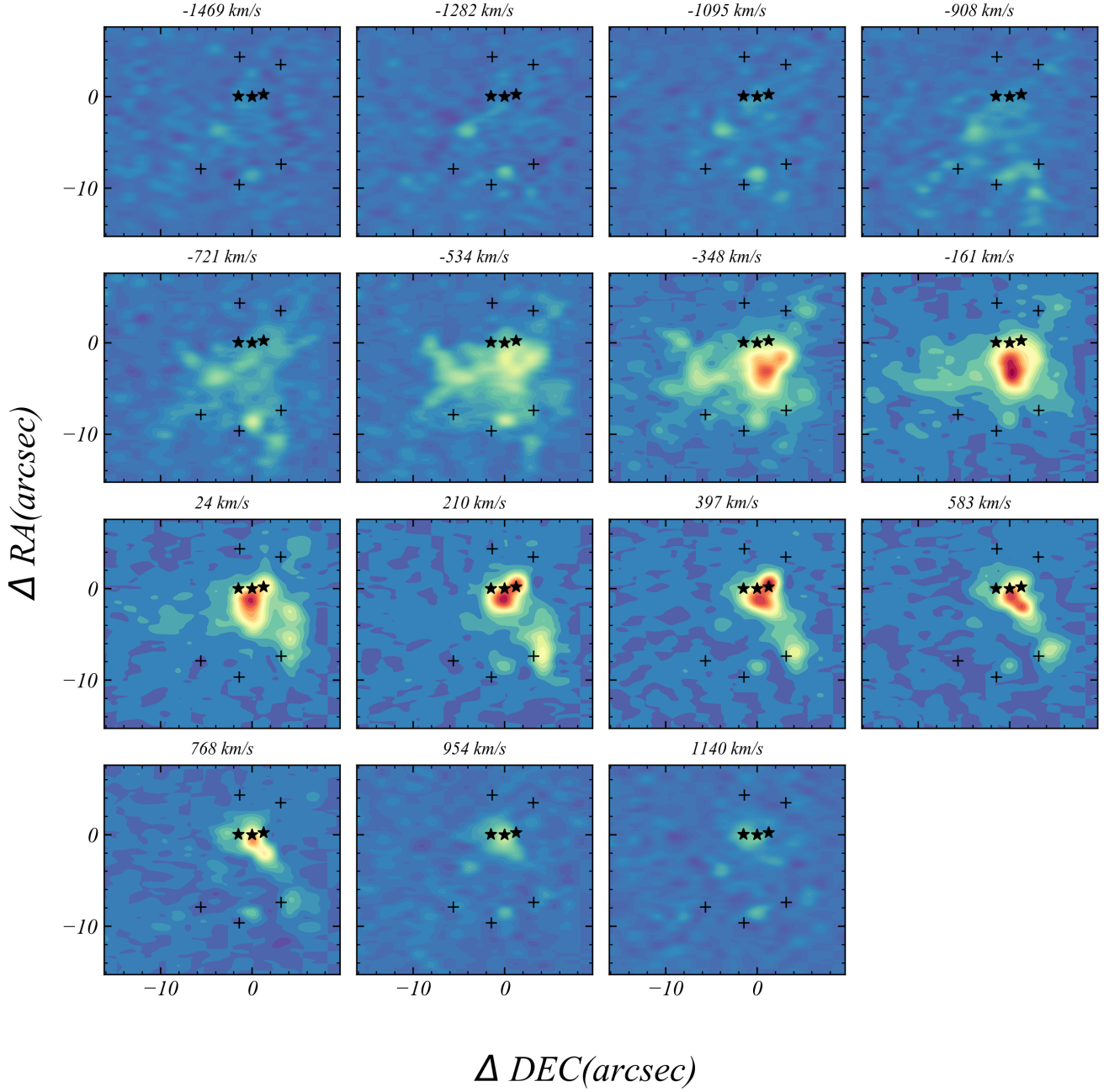


Figure 3: Kinematics of cool gas. It shows signal of $Ly\alpha$ emission at different velocities. We select $\Delta v = 187\text{km/s}$ which corresponds 4\AA as the bin size of these slices. We extract these slices within the range $4000\text{\AA} - 4040\text{\AA}$, for each image here, we use the mean velocity of the bin as title for each image. It shows significant red and blue component on either side of source-B.

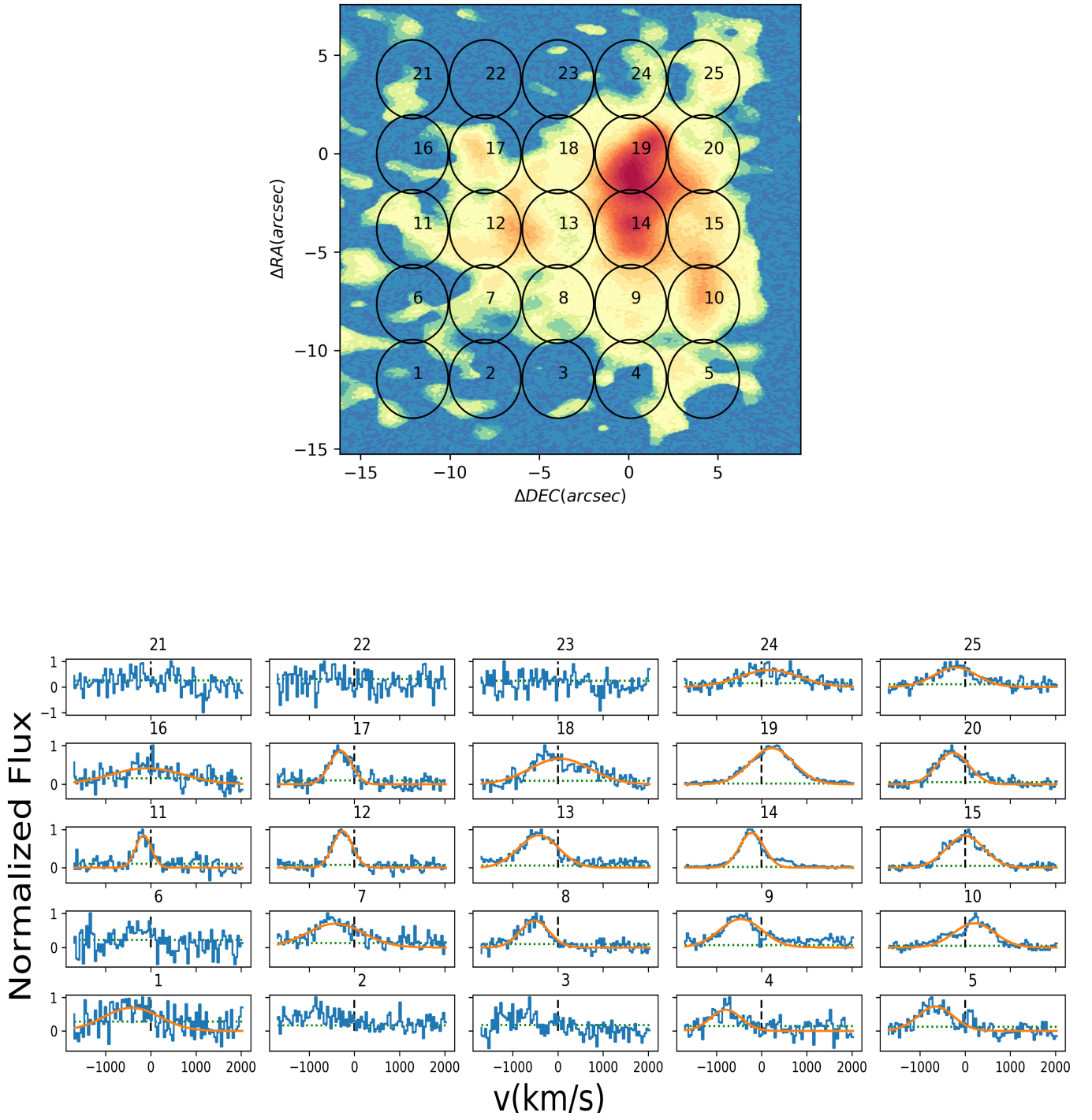


Figure 4: Up: Continuum-subtracted pseudo narrow band image of $Ly\alpha$. We overlay circles on it and number them from 1 to 25. Low: Continuum-subtracted spectra extracted from individual spatial regions indicated in upper panel. The apertures are circle with radius of $2arcsec^2$. We number the spectra from 1 to 25 which corresponds to circles in upper panel. We fit the emission line with single gaussian function and show it with orange lines. The green lines show the noise level calculated from the high-frequency component of spectra.

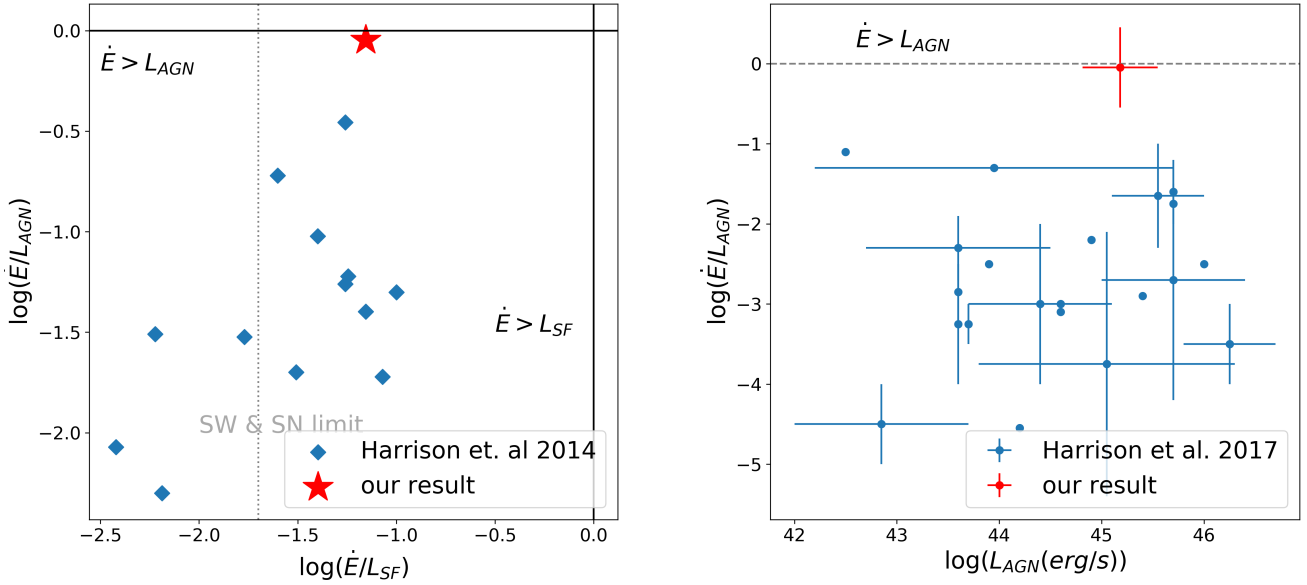


Figure 5: Left: the ratio of our estimated outflow kinetic energy rates (E_{out}) to the AGN luminosity and to the star formation luminosity for our source (red) and sources from Harrison et al. (2014). The dashed vertical line is the estimated maximum mechanical input expected from supernovae and stellar winds. The two solid lines show the coupling efficiency of 1. Right: Observationally determined kinetic coupling efficiencies in Harrison et al. (2018) and our result. The vertical lines show the range of values quoted or, in the case of an error bar, the quoted error on the average value. The horizontal lines show the range of bolometric luminosity for each sample. The dotted line shows coupling efficiency of 1.

coupling efficiency is $\dot{E}_{out}/L_{IR,SF} \approx 0.02$, we indicate this upper limit with gray dot line in Fig.???. Based on this results, stellar winds and supernovae are unlikely to be fully responsible for the observed outflows. On the other hand, the coupling efficiency for AGN-driven case is too large which is close to 1. In the right panel of Fig.?? it shows that if the outflow is driven by AGN, it has already exceed other results with similar AGN luminosity.

Besides, if we instead consider a momentum-driven wind with momentum deposition from the radiation pressure of stars or AGN, the momentum loading factor $f_p = \log(c\dot{P}_{out}/L)$ is $f_{p,SF} = 1.7$ and $f_{p,AGN} = 3.2$ respectively. Nevertheless Zubovas (2018) suggests that a typical momentum loading factor for star-formation-driven case is $f_{p,SF} < 1.4$ which is lower than our estimation, this comparison also rules out the star-formation case. In the same way, we also find that $f_{p,AGN}$ is larger than the typical value.

Moreover, Shankar et al. (2006) mentions the two sources of feedback are important over different mass ranges, in particular, stellar feedback regulates the processes in low-mass galaxies while large galaxies are mainly regulated by AGN feedback. The transition mass for this two feedback mechanisms is $M_{tr} \approx 2 \times 10^{10} M_\odot$. By fitting the SED of source-B, Arrigoni Battaia et al. (2018) estimates its stellar mass of source-B to be $\log(M_{star}/M_\odot) = 11.4^{+0.3}_{-0.2}$. Comparing with M_{tr} , this results also suggests that feedback from star formation is not the dominant reason for the outflow.

However, Zubovas (2018) also suggests there are mechanisms to reach high coupling efficiency and momentum loading factor. One possibility is hyper-Eddington SMBH growth during Compton-thick (heavily obscured) phases. In this case, SMBH would accrete material with extremely large rate and may lead to ultra fast outflows(UFO). Tombesi et al. (2013) shows that this outflow can reach the velocity $\approx 0.1c$ and will have a strong coupling with the interstellar medium(ISM). Fig.6 of Tombesi et al. (2013) shows some coupling efficiency of some UFOs ≈ 1 , but he also explains that this extremely fast and powerful outflow would occur only very close to SMBH $R \approx 1000r_s$ (where r_s is the schwarzschild radius.). He indicates that the large coupling efficiency is probably due to large environment column density $\approx 10^{24} cm^{-2}$ and highly ionized state. These two factors are consistent with the large-scale environmental conditions(MAMMOTH-1, extreme overdensities; enomous lyman α nebula.). Nevertheless, Cai et al. (2017) suggests that the hydrogen column density is in the range $\approx 10^{20} cm^{-2}$, we indicate here that the column density in CGM maybe $10^3 cm^{-2}$ larger than this value.

In summary, based on our analyses we find the outflow is unlikely powered by star-forming processes, but we do see some similar behaviors between the outflow and UFO(high coupling efficiency and high momentum loading factor), so we conclude that this outflow maybe driven by accretion-disc winds. Although there's large uncertainty coupling efficiency estimation, this large coupling efficiency and momentum loading factor have never been seen on such a large scale. From the observation it's still unclear what kind of mecha-

nism leads to such large coupling efficiency on such large scale(the typical coupling efficiency beyond 10kpc < 0.01), it maybe results from large column density $> 10^{24} cm^{-2}$ or very efficient cooling mechanism. Besides, it provides evidence that outflow from central quasar can truly have influence on the protocluster.

4.2. Galaxies merger

By the submillimeter observation with ALMA and data collection from literature, Arrigoni Battaia et al. (2018) fits the spectral energy distribution(SED) for Source-B, as a results he indicates that Source-B is an Ultra-Luminous Infrared Galaxy(ULIRG) with extreme far-infrared luminosity. Besides, Treister et al. (2010) shows that there is substantial observational evidence that ULIRGs(heavily obscured galaxies) are the product of the gas-rich merger of two massive galaxies. Cai et al. (2017) also shows Source-B is a strongly obscured source. On the other hand the the flux-weighted dispersion map of Ly α emission also shows velocity dispersion $> 600 km/s$ corresponding to FWHM $> 1400 km/s$ near Source-B and the large dispersion extent to projected scale $\approx 100 kpc$ (include G-5). Moreover, MAMMOTH-1 is an extreme overdensity($\delta = 10.8 \pm 2.6$). The three sources of source-B is within 70 kpc. All of these evidences suggests a strong galaxies merger in this region.

We suggest that the physical picture of this area is like this: three sources of source-B is experiencing galaxy merger, center source accretes gas and material the other two sources, its super massive black hole(SMBH) is going through a period of rapid growth and produce strong outflow. Owing to the tidal effect between the three sources, lots of material is pulled out from galaxies to CGM. This can also explain why there's such large coupling efficiency between outflow and environment.

Futhermore, from the velocity and dispersion map we see that the region with large dispersion extent to G-5 and there's also obvious velocity gradient on either side of G-5. This clue indicates that there may be also outflow from G-5. The large dispersion also support this point.

5. Conclusions

References

- Arrigoni Battaia, F., Hennawi, J. F., Prochaska, J. X., Oñorbe, J., Farina, E. P., Cantalupo, S., & Lusso, E. 2018, Monthly Notices of the Royal Astronomical Society, 482, 3162
- Cai, Z. et al. 2017, The Astrophysical Journal, 837, 71
- Emonts, B. H., Cai, Z., Prochaska, J. X., Li, Q., & Lehnert, M. D. 2019, The Astrophysical Journal, 887, 86
- Harrison, C., Alexander, D., Mullaney, J., & Swinbank, A. 2014, Monthly Notices of the Royal Astronomical Society, 441, 3306
- Harrison, C., Costa, T., Tadhunter, C., Flötsch, A., Kakkad, D., Perna, M., & Vietri, G. 2018, Nature Astronomy, 2, 198
- Heckman, T. M., Armus, L., Miley, G. K., et al. 1990, Astrophysical Journal Supplement Series, 74, 833

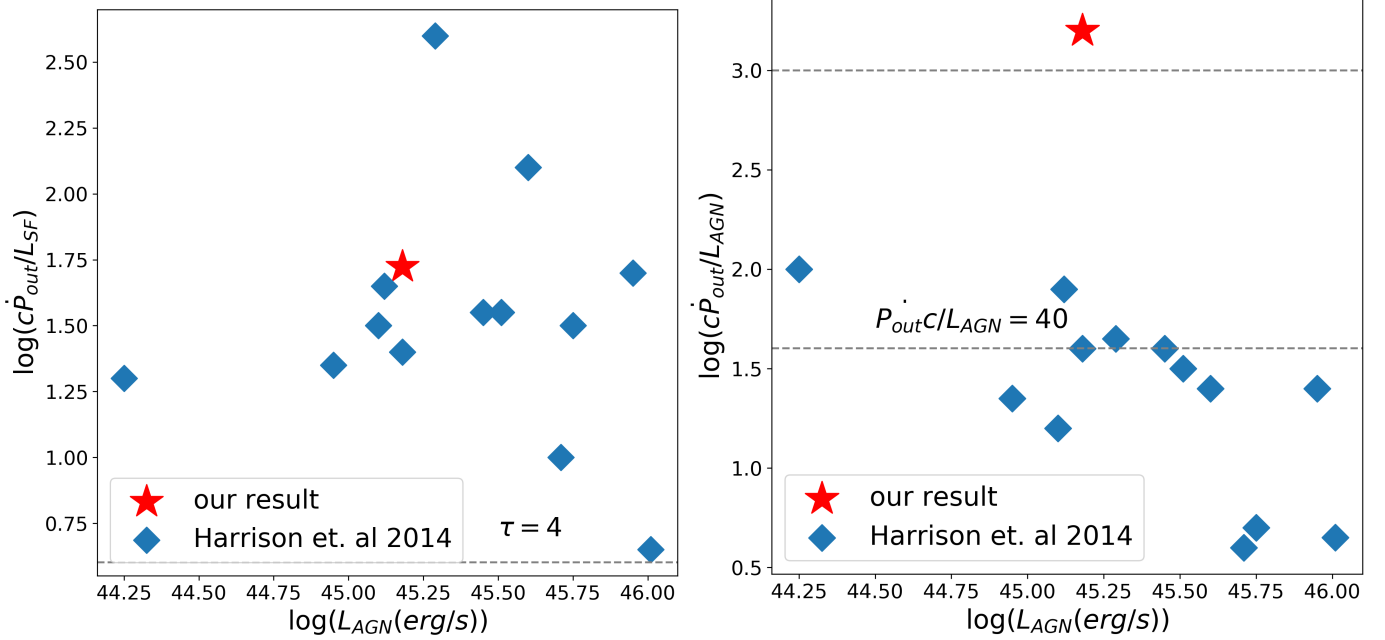


Figure 6: Left: momentum rates of the outflows (\dot{P}_{out} normalized to the star formation luminosity L_{SF}/c versus AGN luminosity. The dashed lines represent the required optical depths if the outflows are driven by radiation pressure from star formation. Right: momentum rate of outflows normalized to AGN luminosity (L_{AGN}/c) versus AGN luminosity. Based on our assumptions, the outflows are unlikely to be purely radiatively driven, the ratio is also too high for theoretical predictions of energy-driven outflows launched by AGN accretion-disc wind.

Kennicutt Jr, R. C. 1998, Annual Review of Astronomy and Astrophysics, 36, 189
 Rodriguez Zaurin, J., Tadhunter, C., Rose, M., & Holt, J. 2013, Monthly Notices of the Royal Astronomical Society, 432, 138
 Shankar, F., Lapi, A., Salucci, P., De Zotti, G., & Danese, L. 2006, The Astrophysical Journal, 643, 14
 Storey, P., & Hummer, D. 1995, Monthly Notices of the Royal Astronomical Society, 272, 41

Tombesi, F., Cappi, M., Reeves, J., Nemmen, R., Braito, V., Gaspari, M., & Reynolds, C. 2013, Monthly Notices of the Royal Astronomical Society, 430, 1102
 Treister, E., Natarajan, P., Sanders, D. B., Urry, C. M., Schawinski, K., & Kartaltepe, J. 2010, Science, 328, 600
 Zubovas, K. 2018, Monthly Notices of the Royal Astronomical Society, 479, 3189